



# Robust three-dimensional porous rGO aerogel anchored with ultra-fine $\alpha$ -Fe<sub>2</sub>O<sub>3</sub> nanoparticles exhibit dominated pseudocapacitance behavior for superior lithium storage



Cong Wu<sup>a</sup>, Yanan Xu<sup>a</sup>, Liyuan Ao<sup>a</sup>, Kai Jiang<sup>a</sup>, Liyan Shang<sup>a</sup>, Yawei Li<sup>a</sup>, Zhigao Hu<sup>a, b, c, \*</sup>, Junhao Chu<sup>a, b, c</sup>

<sup>a</sup> Technical Center for Multifunctional Magneto-Optical Spectroscopy (Shanghai), Department of Materials, School of Physics and Electronic Science, East China Normal University, Shanghai, 200241, China

<sup>b</sup> Collaborative Innovation Center of Extreme Optics, Shanxi University, Taiyuan, Shanxi, 030006, China

<sup>c</sup> Shanghai Institute of Intelligent Electronics & Systems, Fudan University, Shanghai, 200433, China

## ARTICLE INFO

### Article history:

Received 18 July 2019

Received in revised form

6 October 2019

Accepted 9 October 2019

Available online 15 October 2019

### Keywords:

Porous structure

Pseudocapacitance behavior

Iron oxide

Rate performance

Lithium-ion battery

## ABSTRACT

Based on the ultra-fast faradaic surface induced reversible redox reactions, pseudocapacitance behavior with rapid electrochemical kinetics can boost the high power density of lithium ion battery. In this work, a three-dimensional (3D) interconnected porous reduced graphene oxide network incorporated with homogeneously dispersed ultra-fine  $\alpha$ -Fe<sub>2</sub>O<sub>3</sub> nanoparticles (denoted  $\alpha$ -Fe<sub>2</sub>O<sub>3</sub>@3DrGO) is subtly synthesised through a facial hydrothermal self-assembly process. Such desirable hierarchical structure delivers an ever-increasing pseudocapacitance storage as anode, achieving an unprecedented rate capacity (921.6, and 812.4 mA h g<sup>-1</sup> at 1 and 5 A g<sup>-1</sup>) and a superior cycle performance with ultra-high capacity (1198.6 mA h g<sup>-1</sup> at 1 A g<sup>-1</sup> over 200 cycles), which is almost the best result reported so far. Even at a high current density of 5 A g<sup>-1</sup>, it still maintains the excellent cycle stability with a capacity of 396.6 mA h g<sup>-1</sup> after 2000 cycles. Such outstanding electrochemical performance may be ascribed to the synergy of the robust structure, porous surface morphology as well as accompanying dominated pseudocapacitance behavior. We hope this work can provide a novel strategy for realizing high rate and stable cycle performances in lithium storage.

© 2019 Elsevier B.V. All rights reserved.

## 1. Introduction

With the development of technology, lithium-ion batteries (LIBs) have been evolved into the protagonist of currently portable electronic device market, and gradually expanded to large-scale applications, such as electric vehicles and smart electricity grid storage [1–3]. However, the commercial LIBs mainly employ graphene with low capacity of 372 mA h g<sup>-1</sup> as a negative electrode nowadays, which cannot satisfy the current demand for high power density, high energy density and long life-span in LIBs field. It prompts that a lot of efforts have been invested in exploring advanced new anode materials with

superior electrochemical performance, such as graphite carbon, metal, transition metal oxides (TMOs) or sulfides (TMSs) [4–13]. Among them, TMOs with high theoretical capacity are considered as future potential anode candidates, where more than one electron transfer per formula unit involving in the conversion process. Particularly, Fe<sub>2</sub>O<sub>3</sub> delivers a high theoretical capacity of 1007 mA h g<sup>-1</sup> according the conversion process: Fe<sub>2</sub>O<sub>3</sub> + 6Li<sup>+</sup> + 6e<sup>-</sup> → 2Fe + 3Li<sub>2</sub>O. Moreover, the merits of low consumption, abundant resources, non-toxicity, improved safety and environmental friendliness make it arise widespread concern of researchers. Till now, various kinds of Fe<sub>2</sub>O<sub>3</sub> have been fabricated and used in LIBs, such as maghemite ( $\gamma$ -Fe<sub>2</sub>O<sub>3</sub>), magnetite (Fe<sub>3</sub>O<sub>4</sub>) and hematite ( $\alpha$ -Fe<sub>2</sub>O<sub>3</sub>). Unfortunately, there are still many problems existing in the practical applications of Fe<sub>2</sub>O<sub>3</sub> anode. Firstly, the sluggish kinetics induced by inherently poor electronic and ionic conductivity cannot meet the demand for adequate and rapid lithiation/delithiation processes. Secondly, severe volume

\* Corresponding author. Technical Center for Multifunctional Magneto-Optical Spectroscopy (Shanghai), Department of Materials, School of Physics and Electronic Science, East China Normal University, Shanghai, 200241, China.

E-mail address: [zghu@ee.ecnu.edu.cn](mailto:zghu@ee.ecnu.edu.cn) (Z. Hu).

changes during charging and discharging process tend to induce agglomeration of the active material and destruction of the electrode, which is detrimental to long cycle stability. Besides, there is no good structural framework to provide multi-dimensional accessible transport paths for lithium ions, and active materials cannot be sufficiently utilized [14–16]. Therefore, equipping with a good morphological structure is the necessary condition for achieving excellent electrochemical performance.

So far, for curing the above issues, great efforts have been invested to the beneficial morphology design and the coupling with the conductive framework to achieve the excellent electrochemical performance for iron oxide anodes. The sandwiched graphene sheets inserted with yolk-shell  $\gamma$ - $\text{Fe}_2\text{O}_3$  nanoparticles encapsulated by graphene shells was prepared by Zhang et al. [17]. The capability of which was  $737 \text{ mA h g}^{-1}$  when the current density was increased to  $1 \text{ A g}^{-1}$ . P. Santhoshkumar et al. reported that the three-dimensional (3D) iron oxide ( $\alpha$ - $\text{Fe}_2\text{O}_3$ ) sub-micron particles were synthesised through one-pot hydrothermal approach. As anode in LIB, they delivered a high reversible capacity of  $968 \text{ mA h g}^{-1}$  at  $0.1 \text{ A g}^{-1}$  after 100 cycles [18]. Moreover, spider-web-like MWCNT/ $\gamma$ - $\text{Fe}_2\text{O}_3$  composite network was obtained by Bhattacharya et al. and this composite showed a specific capacity of  $\approx 822 \text{ mA h g}^{-1}$  at  $50 \text{ mA g}^{-1}$  [19]. Cho et al. reported a bubble-nanorod-structured  $\text{Fe}_2\text{O}_3$  carbon nanofibers as advanced anode material for LIBs and at the end of 300 cycles they displayed a specific capacity of  $812 \text{ mA h g}^{-1}$  at a  $1 \text{ A g}^{-1}$  rate [20]. Besides, Zhang et al. obtained quasi 1D  $\text{Fe}_2\text{O}_3$ -carbon composite nanofibers by the electro-spinning method as anode for LIBs, the composite exhibited a reversible capacity of  $820 \text{ mA h g}^{-1}$  at  $0.2 \text{ A g}^{-1}$  up to 100 cycles [21].

In spite of the good structural characteristics, intrinsically sluggish solid-state lithium diffusion still limits its electrochemical performance. As we know, pseudocapacitance behavior signifies a kind of ultra-fast electrochemical reaction mechanism derived from the surface-induced capacitive process, which is definitely different from the faradaic solid phase diffusion controlled process. Pseudocapacitance storage could greatly increase high rate capacity and maintain long-term cycle stability through continuous and fast reversible faradaic charge-transfer reactions including redox reactions on the surface of electrode material as well as swiftly bulk lithium ion intercalation/deintercalation, especially for transition metal oxide anodes [22–25]. To this end, such dominated pseudocapacitive contributions has been successfully realized in various transition metal sulfides ( $\text{SnS}_2$ ,  $\text{MoS}_2$ ) [26,27] and metal oxides ( $\text{Nb}_2\text{O}_5$ ,  $\text{TiO}_2$ ,  $\text{MoO}_3$ ,  $\text{FeOOH}$ ,  $\text{Fe}_2\text{O}_3$  etc.) [28–32] anodes with outstanding electrochemical performance. Thus, modifying surface pseudocapacitive property to achieve an ultra-fast reaction kinetics is desiderated for  $\text{Fe}_2\text{O}_3$  anode materials.

In this work, a novel  $\alpha$ - $\text{Fe}_2\text{O}_3$ @3DrGO aerogel composite has been successfully obtained through a facial hydrothermal process. The reduced graphene oxide sheets self-assemble to form a three-dimensional interconnected porous framework as the substrate and the ultra-fine  $\alpha$ - $\text{Fe}_2\text{O}_3$  particles are homogeneously anchored on the inner or outside surface of the mesoporous. Beneficial from such superior structure with unique porosity, the conductivity has been significantly improved and lithium ion transmission pathways become more diverse. Meanwhile, the volume expansion effect has been sufficiently suppressed as well as the agglomeration of iron oxide during charging/discharging process has been effectively avoided. Moreover, due to the enlarged accessible surface area, the  $\alpha$ - $\text{Fe}_2\text{O}_3$ @3DrGO electrode reveals a predominant surface-induced pseudocapacitive lithium storage, which greatly improves the high rate capacity, highly reversibility and stable long life-span.

## 2. Experimental section

### 2.1. Synthesis of $\alpha$ - $\text{Fe}_2\text{O}_3$ @3D porous reduced graphene oxide aerogel

Graphene oxide (GO) was prepared from the natural graphite nanosheets by a modified Hummer's method [33]. Typically, 160 mg GO was added to 60 mL deionized (DI) water, magnetic stirred for all day and night. Then it was high-intensively ultrasonicated by an ultrasonication probe (1000 W) for 30 min to form GO colloidal solution. A certain amount of aqueous solution of ferric chloride (20 mL DI water, 3.2 mmol ferric chloride) was slowly poured into above GO solution, stirred for 2 h at room temperature. Next, an appropriate amount of ammonia solution (25 wt%) was dropped into the mixtures by dropwise until the PH value reaching to 10. Thereafter, 110 mg of hydrazine hydrate solution was diluted in 1.5 mL of DI water and added to the above solution at a speed of  $2 \mu\text{L}$  per second under stirring for 30 min. Finally, the mixed solution was transferred to 100 mL Teflon-lined stainless steel autoclave followed by hydrothermal reaction at  $200 \text{ }^\circ\text{C}$  for 10 h. During the high temperature hydrothermal reaction, GO was transformed into reduced graphene oxide. After cooling to room temperature, the resulting products were collected and rinsed by DI water for several times and the black  $\alpha$ - $\text{Fe}_2\text{O}_3$ @3DrGO aerogel was obtained by freeze-drying at minus  $85 \text{ }^\circ\text{C}$  for 30 h. For comparison, the bare  $\alpha$ - $\text{Fe}_2\text{O}_3$  and three-dimensional porous reduce graphene oxide (3DrGO) aerogel were synthesised during the same process without GO, hydrazine hydrate or ferric chloride solution respectively, while keeping the other conditions as invariant. In addition, we have also prepared the  $\alpha$ - $\text{Fe}_2\text{O}_3$ @3DrGO aerogel with different ratios of graphene oxide and  $\alpha$ - $\text{Fe}_2\text{O}_3$ .

### 2.2. Characterization methods

The crystal structures of samples were investigated by X-ray diffraction (XRD, Bruker D8 Advance diffractometer) equipped with  $\text{Cu-K}\alpha$  radiation ( $\lambda = 1.5418 \text{ \AA}$ ) at a generator voltage of 40 KV and generator current of 20 mA from  $10^\circ$  to  $80^\circ$ . Raman spectra were measured by a Jobin-Yvon LabRAM HR 800 micro-Raman spectrometer using a 532 nm air-ion laser. For calculating the fraction of  $\alpha$ - $\text{Fe}_2\text{O}_3$  or carbon in the nanocomposite, the thermogravimetric analysis (TG, TA Instruments 2000) and differential scanning calorimetry (DSC) were carried out over a temperature range from  $30 \text{ }^\circ\text{C}$  -  $800 \text{ }^\circ\text{C}$  in air atmosphere with the heating rate of  $10^\circ\text{C min}^{-1}$ . Brunauer-Emmett-Teller (BET) were measured to investigate the specific surface area and average pore size distribution of nanocomposite (TriStar II 3020, America). The X-ray photoelectron spectroscopy (XPS) analysis was conducted on a RBD upgraded PHI-5000C ESCA system (PerkinElmer) with  $\text{Mg-K}\alpha$  radiation ( $h\nu = 1253.6 \text{ eV}$ ), and binding energies were calibrated by using the containment carbon ( $\text{C } 1s = 284.6 \text{ eV}$ ). To explore the morphologies features of the samples, filed emission scanning electron microscopy (FESEM, JEOL-JSM-6700F) equipped with energy dispersive X-ray spectroscopy (EDS) was performed. In addition, transmission electron microscopy (TEM) and selected area electron diffraction (SAED) studies were employed at a FEI Tecnai G2 F20 instrument with an operating voltage of 200 KV.

### 2.3. Electrochemical measurements

To investigate the electrochemical performance of  $\alpha$ - $\text{Fe}_2\text{O}_3$ @3DrGO aerogel, the CR2025 coin-type half-cell was fabricated in a gloves box full filled with argon gas. The working electrodes were prepared by mixing the as-prepared materials (80 wt %), acetylene black (10 wt%) and polyvinylidene fluoride binder

(10 wt%), which were dissolved in *N*-methyl-2-pyrrolidinone solvent. Then the uniform slurry was coated on the copper foil and dried at 100 °C in a vacuum oven for 12 h and the mass loading of active materials in every anode was about 0.8 mg/cm<sup>2</sup>. The electrolyte consisted of LiPF<sub>6</sub> (1 M) solution, which was dissolved in a 1:1:1 (by volume) mixture of ethylene carbonate, dimethyl carbonate and ethyl methyl carbonate. The lithium foil and Cellgard 2400 were used as the counter electrode and separator respectively. The Galvanostatic charge/discharge rate and cycle performance were performed on a LAND CT 3001A battery test system with a voltage window of 0.01–3.0 V (vs. Li/Li<sup>+</sup>) at various current densities. The cyclic voltammetry (CV) curves were recorded by a CHI660 electrochemical workstation at a series sweep rate over the voltage window of 0.01–3.0 V and the electrochemical impedance spectroscopy (EIS) were also investigated by using CHI660 electrochemical workstation with an amplitude of 5 mV over the frequency range of 0.01 Hz–100 kHz at room temperature.

### 3. Results and discussion

#### 3.1. Microstructures of the prepared sample

As shown in Fig. 1a, the crystal structure, purity and crystalline phase characterizations of as-synthesised materials are well presented. The XRD diffraction peaks located at 24.1°, 33.2°, 35.6°, 40.9°, 49.5°, 54.1°, 57.6°, 62.4°, 64.0°, 72.0°, 75.4° can be indexed to the (012), (104), (110), (113), (024), (116), (018), (214), (300), (1010), (220) crystal faces respectively, which match well with the hematite Fe<sub>2</sub>O<sub>3</sub> rhombohedral phase (space group: R-3c, JCPDS: 33-0664) [34,35]. The average particle size was calculated to be ~ 44.1 nm based on the Scherrer formula. Moreover, the sharp characteristic peaks in both XRD patterns are quite consistent,

indicating the good purity and crystallinity of  $\alpha$ -Fe<sub>2</sub>O<sub>3</sub>. In addition, the broad graphitic characteristic peak (20° - 30°) was not detected, revealing that the  $\alpha$ -Fe<sub>2</sub>O<sub>3</sub> nanoparticles are well fixed on the surface of reduced graphene oxide, which can effectively inhibit the agglomeration of reduced graphene oxide sheets.

Raman spectroscopy of as-synthesised samples are further displayed in Fig. 1b. Two obvious main peaks located at 1328 and 1590 cm<sup>-1</sup>, which are corresponding to disordered D band and graphite G band, respectively. As we know, the D band is assigned to the mode of *k*-point phonon of A<sub>1g</sub> symmetry and the G band is attributed to the first-order scattering of the E<sub>2g</sub> phonon of carbon atom [36,37]. Therefore, the ratios (I<sub>D</sub>/I<sub>G</sub>) of peak intensity between the D and G band can effectively reflect the structure changes of carbon-based materials. The I<sub>D</sub>/I<sub>G</sub> ratio of  $\alpha$ -Fe<sub>2</sub>O<sub>3</sub>@3DrGO is very close to that of 3DrGO (1.78 vs. 1.79), which implies the introducing of disorders and defects after hydrothermal process. Moreover, the  $\alpha$ -Fe<sub>2</sub>O<sub>3</sub>@3DrGO composite still retains the electronic and structural integrity of 3DrGO, which will be favorable to electron transfer in electrochemical process [38]. A series of vibration peaks at low-wavenumber region (100–700 cm<sup>-1</sup>) are magnified in Fig. S1, which can be attributed to A<sub>1g</sub> (220, 490 cm<sup>-1</sup>), E<sub>g</sub> (285, 397 and 597 cm<sup>-1</sup>) vibration modes of  $\alpha$ -Fe<sub>2</sub>O<sub>3</sub> crystal [39].

To explore the stability and carbon content of  $\alpha$ -Fe<sub>2</sub>O<sub>3</sub>@3DrGO composite, TG-DSC analysis is exhibited in Fig. 1c. An obvious weight loss with prominent endothermic peak can be seen in the temperature range of 250 °C - 600 °C. It reveals that the rGO starts oxidization to form gaseous species at 250 °C and burns completely at 600 °C, only leaving behind  $\alpha$ -Fe<sub>2</sub>O<sub>3</sub> residual. The TG-DSC data confirms that the weight percentage of carbon and  $\alpha$ -Fe<sub>2</sub>O<sub>3</sub> in this composite are ~ 21.6 wt% and 78.4 wt%, respectively.

Nitrogen adsorption/desorption isotherms are obtained to analyze the specific surface area and porosity of the  $\alpha$ -

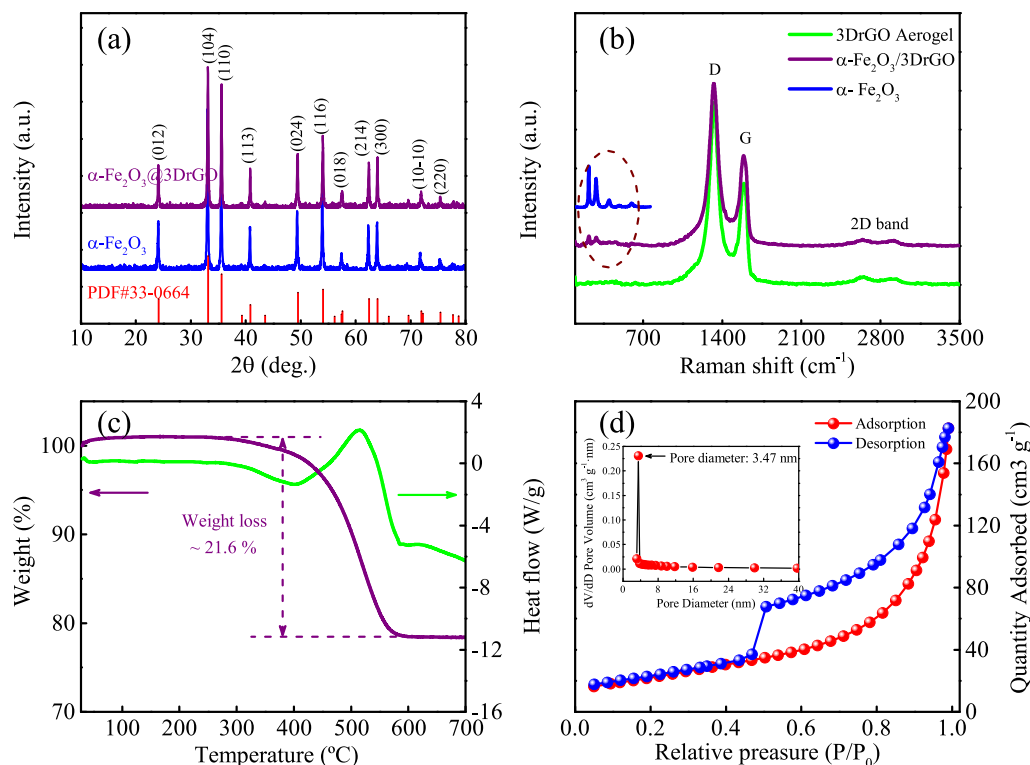


**Fig. 1.** (a) XRD patterns of  $\alpha$ -Fe<sub>2</sub>O<sub>3</sub>,  $\alpha$ -Fe<sub>2</sub>O<sub>3</sub>@3DrGO; (b) Raman spectra of as-synthesised nanocomposites; (c) TG-DSC analysis of  $\alpha$ -Fe<sub>2</sub>O<sub>3</sub>@3DrGO and 3DrGO; (d) N<sub>2</sub> adsorption-desorption isotherms of  $\alpha$ -Fe<sub>2</sub>O<sub>3</sub>@3DrGO (The inset shows the corresponding pore size distribution).

$\text{Fe}_2\text{O}_3@3\text{DrGO}$  material. In Fig. 1d, on account of the capillary condensation, the isotherm rises quickly with increasing the  $P/P_0$  as well as the curves of absorption and desorption separate from each other. The whole isotherm exhibits the type IV hysteresis loop, which demonstrates the mesoporous properties of as-synthesised material. The specific surface area of  $\alpha\text{-Fe}_2\text{O}_3@3\text{DrGO}$  composite is about  $82.0\text{ m}^2\text{ g}^{-1}$  based the BET results. In the illustration, the pore-size distribution is estimated to be  $3.47\text{ nm}$  according to the Barrett-Joyner-Halenda (BJH) method. Such mesoporous structure along with a high surface area can effectively promote rapid diffusion of lithium ion and deep penetration of electrolyte. Besides, the porosity can provide numerous active sites for lithium storage. Furthermore, it can also relieve the volume expansion during the lithium insertion and extraction process, which will significantly improve the specific capacity and long cycling stability.

In order to further investigate the surface chemical composition of resulting  $\alpha\text{-Fe}_2\text{O}_3@3\text{DrGO}$  material and the valence state of various element, XPS measurements are performed. The entire survey XPS spectrum (Fig. S2) indicates the existence of Fe, O, N and C elements in the as-synthesised product without any other impurity elements. As presented in Fig. 2a, the high-resolution C 1s spectrum can be divided into four peaks at  $284.7\text{ eV}$ ,  $285.4\text{ eV}$ ,  $286.3\text{ eV}$  and  $288.2\text{ eV}$ , ascribing to the bonds of non-oxygenated C-C/C=C, C-O/C-N, C=O, HO-C=O, respectively [40,41]. The dominated non-oxygenated C peak ensures the good electrical conductivity of  $\alpha\text{-Fe}_2\text{O}_3@3\text{DrGO}$ . Furthermore, the O 1s spectrum in Fig. 2b can be deconvoluted into three peaks to show the presence of the lattice oxygen ( $530.2\text{ eV}$ ), hydroxide ions/carbonate species ( $530.8\text{ eV}$ ) and C-O/O=C-O functional groups ( $532.3\text{ eV}$ ) in reduced graphene oxide [42]. Fig. 2c displays two dominated characterize peaks: Fe  $2p_{3/2}$  and Fe  $2p_{1/2}$  with the binding energy of  $711.4$  and  $725.0\text{ eV}$ , respectively. Besides, two additional satellite

peak located at  $719.6\text{ eV}$  and  $732.7\text{ eV}$  are ascribed to the purely trivalent nature, manifesting that the Fe element mainly exhibits the form of iron(III) in the resulting composite [43,44]. Fig. 2d shows the N-doping for this composite with the introduction of  $\text{NH}_3\cdot\text{H}_2\text{O}$  and hydrazine hydrate during the hydrothermal reaction. The high resolution N 1s spectrum can be fitted into three peaks at  $398.8$ ,  $400.3$  and  $402.3\text{ eV}$ , assigning to the pyridinic N, pyrrolic N and quaternary N [45,46]. Nitrogen doping can enhance the polarity of graphene surface, which will be favorable for attracting  $\alpha\text{-Fe}_2\text{O}_3$  nanoparticles and providing more nucleation growth sites. Moreover, it can also improve electrical conductivity and facilitate electron transport.

The  $\alpha\text{-Fe}_2\text{O}_3@3\text{DrGO}$  composite was synthesised through a facial hydrothermal process, as schematically illuminated in Fig. 3a. Firstly, for preparing a uniformly dispersed graphene oxide suspension, the GO aqueous solution was stirred for a certain amount of time and subjected to ultra-high power ultrasonic treatment. Then, the multi-layer graphene oxide was broken into pieces and exfoliated into single or few-layer. As we know, graphene surface is filled with numerous negatively charged oxygen-containing functional groups. When  $\text{Fe}(\text{NO}_3)_3\cdot 9\text{H}_2\text{O}$  precursors were sufficiently mixed in above suspension, the hydrolyzed metal cations  $\text{Fe}^{3+}$  were attracted to the functional groups with the aid of electrostatic interaction, which may act as nucleation growth sites. As the reaction proceeded further, the  $\alpha\text{-Fe}_2\text{O}_3$  nanoparticles were grown up and firmly anchored on the surface of GO. Furthermore, these uniform nanoparticles can prevent GO from stacking together. Meanwhile, graphene oxide sheets were connected to each other to form a three-dimensional porous structure, effectively preventing the agglomeration of nanoparticles. At the same time, the porous structure can provide more growth sites for  $\alpha\text{-Fe}_2\text{O}_3$ . In the end, both of them supplemented each other and came into being a

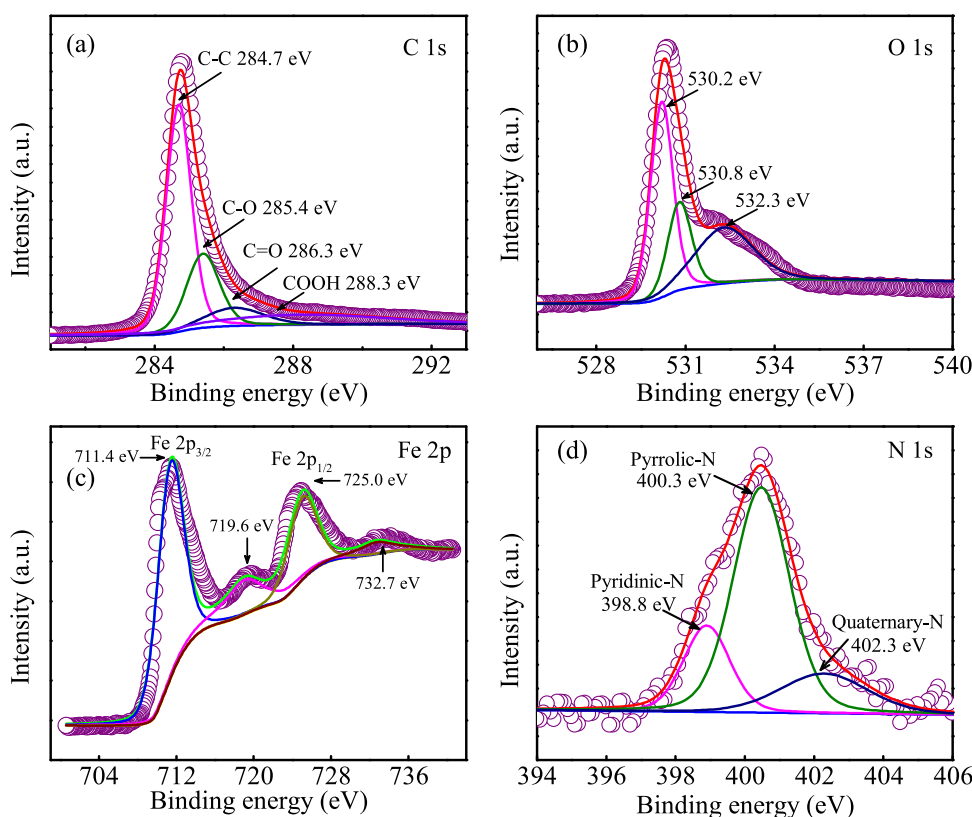
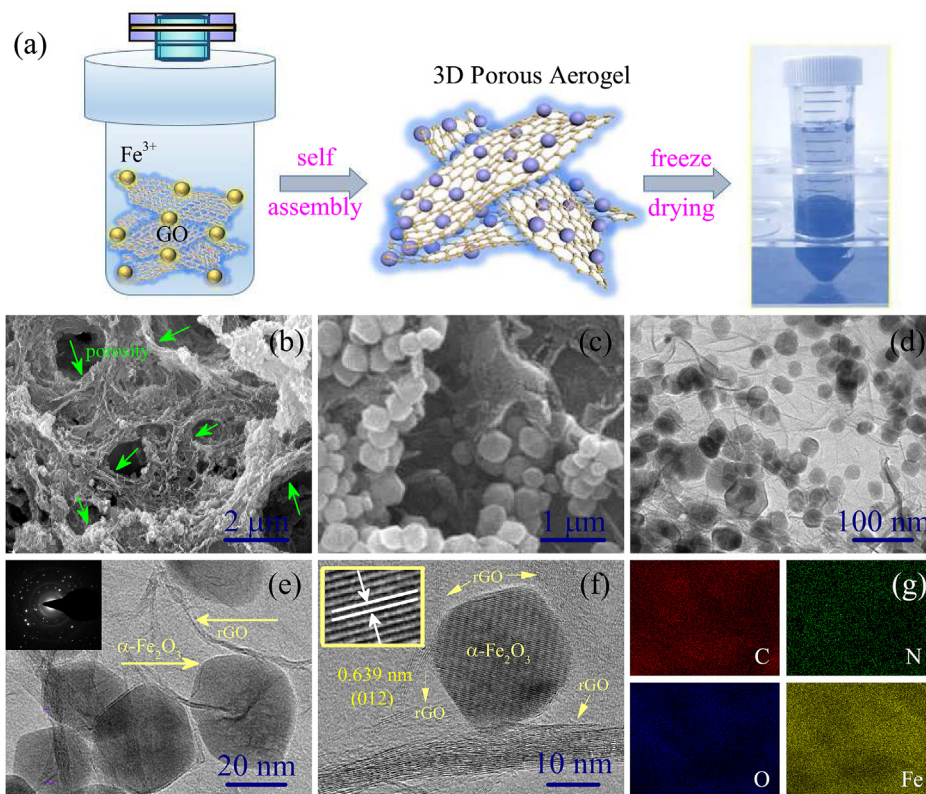


Fig. 2. (High resolution XPS spectrum of  $\alpha\text{-Fe}_2\text{O}_3@3\text{DrGO}$  nanocomposite: (a) C 1s, (b) O 1s, (c) Fe 2p and (d) N 1s, respectively.



**Fig. 3.** (a) Schematic illustration of the synthesis process for  $\alpha\text{-Fe}_2\text{O}_3@3\text{DrGO}$  nanocomposite; (b) typical SEM image and (c) high-magnification SEM image of  $\alpha\text{-Fe}_2\text{O}_3@3\text{DrGO}$ . The green arrows indicate the porous structure feature; (d) TEM image and (e) high-magnification TEM image of  $\alpha\text{-Fe}_2\text{O}_3@3\text{DrGO}$ . The inset image of (d) shows the SAED pattern; (f) HRTEM image of  $\alpha\text{-Fe}_2\text{O}_3@3\text{DrGO}$ ; (g) elemental mapping images of C, N, O and Fe for  $\alpha\text{-Fe}_2\text{O}_3@3\text{DrGO}$ . (For interpretation of the references to colour in this figure legend, the reader is referred to the Web version of this article.)

stable three-dimensional porous composite under the synergist effect.

To explore the morphology and microstructure of obtained materials, SEM and TEM characterization were performed. Fig. S3 shows that  $\alpha\text{-Fe}_2\text{O}_3$  presents dense morphology constructed by closely stacked nanoparticles with the size of  $\sim 50$  nm, approximated with the calculation results of the Scherrer formula. These small particles will be beneficial to the lithiation reaction. Fig. S4 displays the uniformly distributed single-layer or few-layer states of GO sheets. Furthermore, interconnected flakes assembled into a three-dimensional hierarchical porous architecture with super mesoporous. Apparently, after the ingenious combination of these beneficial features,  $\alpha\text{-Fe}_2\text{O}_3@3\text{DrGO}$  hybrid exhibits a similar structure with an integrated interconnected framework (Fig. 3b). It's noteworthy that it can not only facilitate the self-assembly of GO flakes, but also serve as a linker between GO for forming more mesopores (indicated by arrow), which is consistent with the large hysteresis loop of  $\text{N}_2$  adsorption-desorption isotherms. In the high-magnification SEM image of  $\alpha\text{-Fe}_2\text{O}_3@3\text{DrGO}$  (Fig. 3c), the small particles are distinguishably decorated on graphene flakes whether inside or outside the pore. Such integrated porous structure could promote deep penetration of electrolyte, accelerates ion diffusion, and also effectively alleviate volume expansion during the discharge/charge process. At the same time, the forming 3D conductive framework can realize faster electronic transfer among  $\alpha\text{-Fe}_2\text{O}_3$  particles, GO and the current collectors. In Fig. 3d, the TEM images of  $\alpha\text{-Fe}_2\text{O}_3@3\text{DrGO}$  nanocomposite further demonstrate that the  $\alpha\text{-Fe}_2\text{O}_3$  nanoparticles are well distributed and encapsulated by corrugated graphene flakes. Moreover, the graphene marked by the arrow in Fig. 3e is thin and transparent, manifesting

a single-layer or few-layer graphene, consisting with SEM results. In the high resolution TEM (HRTEM) image (Fig. 3f), the interface interaction between rGO layer and  $\alpha\text{-Fe}_2\text{O}_3$  nanoparticle are well presented. As the arrows point, it's distinct that the  $\alpha\text{-Fe}_2\text{O}_3$  nanoparticle is firmly anchored on the surface of rGO. The illustration in Fig. 3f clearly demonstrates that the interplanar distance between the lattice fringes is  $3.69 \text{ \AA}$ , corresponding to the characteristic interlayer spacing of (012) facet in single-crystalline trigonal  $\alpha\text{-Fe}_2\text{O}_3$ . From the EDS elemental mapping (Fig. 3g) analysis, the well distribution of C, N, O and Fe elements further confirms that  $\alpha\text{-Fe}_2\text{O}_3$  particles are uniformly anchored on the reduced graphene oxide framework.

### 3.2. Electrochemical performance of the prepared samples

In order to explore the effect of such 3D porous structure on electrochemical performance, the  $\alpha\text{-Fe}_2\text{O}_3@3\text{DrGO}$  composite was evaluated in half-cells with Li foil as the counter electrode. Fig. 4a exhibits the galvanostatic discharge/charge curves of  $\alpha\text{-Fe}_2\text{O}_3@3\text{DrGO}$  electrode for the 1st, 2nd, 5th, and 30th cycle at a current density of  $0.1 \text{ A g}^{-1}$  between 0.01 and 3.0 V versus Li/Li<sup>+</sup>. In the discharge profile of the first cycle, the voltage drops rapidly from the initial state to 0.85 V and presents a long voltage stage. It can be assigned to the insertion of lithium ion into the crystalline structure of  $\alpha\text{-Fe}_2\text{O}_3$  and the formation of solid electrolyte interphase (SEI) layer [47]. Additionally, there is a distinguishable slope appearing from 0.75 to 0.01 V. This may be related to the lithium ion insertion into graphene carbon, reflecting the capacity contribution of carbon composition [48]. During the charge process, the curve firstly exhibits a smooth rise (0.01–1.4 V), followed by a tilted

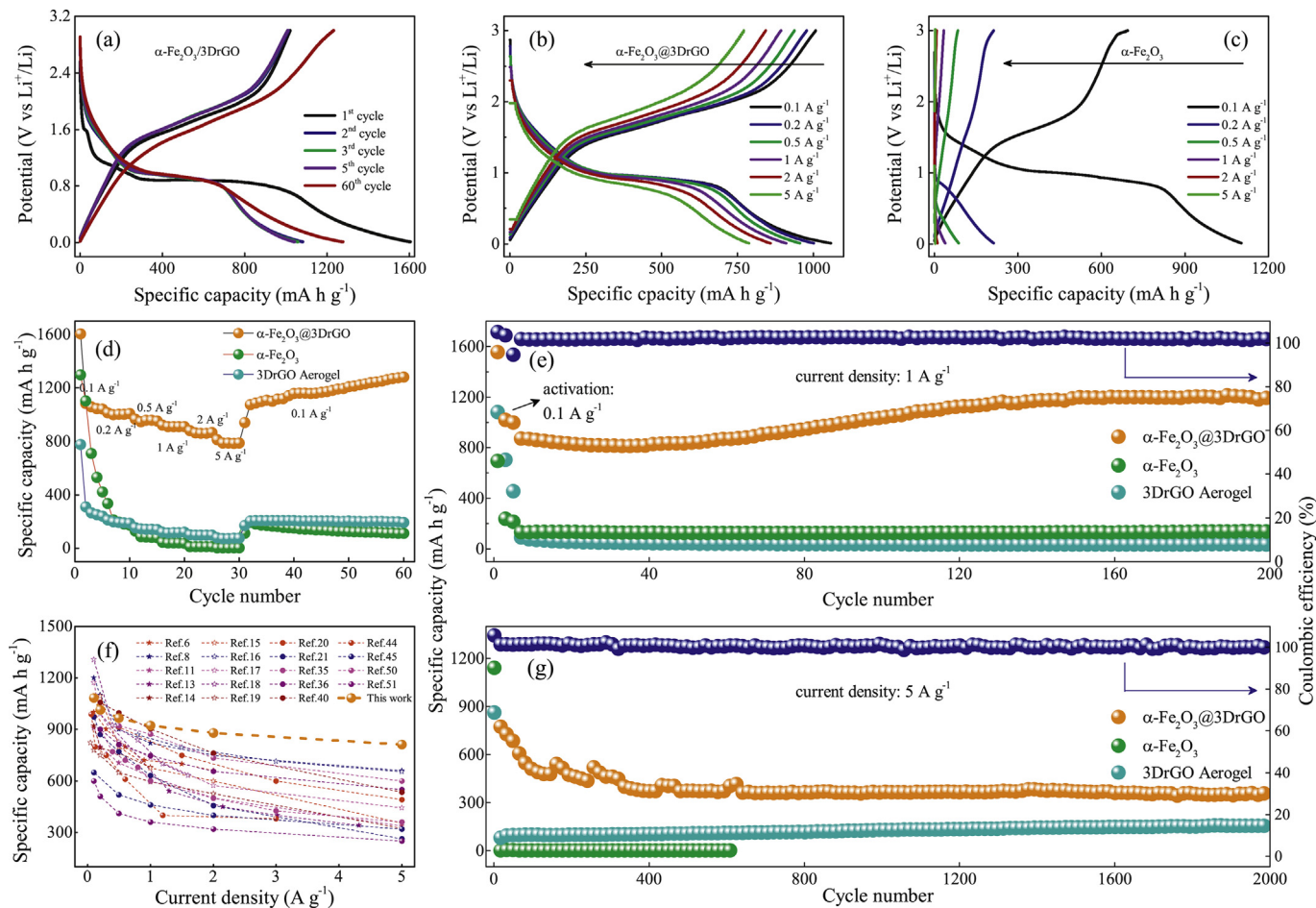


**Fig. 4.** (a) Galvanostatic charge/discharge profiles of  $\alpha\text{-Fe}_2\text{O}_3@3\text{DrGO}$  electrode for initial 5 cycles at a current density of  $0.1 \text{ A g}^{-1}$ ; (b)–(c) Galvanostatic charge/discharge profiles of  $\alpha\text{-Fe}_2\text{O}_3@3\text{DrGO}$  and  $\alpha\text{-Fe}_2\text{O}_3$  electrodes at various current densities from  $0.1$  to  $5 \text{ A g}^{-1}$ ; (d) Rate performance of  $\alpha\text{-Fe}_2\text{O}_3@3\text{DrGO}$ ,  $\alpha\text{-Fe}_2\text{O}_3$  and  $3\text{DrGO}$  electrodes at various current densities from  $0.1$  to  $5 \text{ A g}^{-1}$ ; (e) and (g) Cycling performance of  $\alpha\text{-Fe}_2\text{O}_3@3\text{DrGO}$ ,  $\alpha\text{-Fe}_2\text{O}_3$  and  $3\text{DrGO}$  electrodes cycled at  $1 \text{ A g}^{-1}$  for 200 cycles and at  $5 \text{ A g}^{-1}$  for 2000 cycles (initial 5 cycles at  $0.1 \text{ A g}^{-1}$  for activation); (f) The rate performance comparisons of materials in this work and previous iron oxide based work in the literature.

voltage platform (1.4–2.1 V) and ends with a steep rise (2.1–3.0 V). The tilted voltage platform corresponds to the oxidation of metallic Fe to  $\text{Fe}_2\text{O}_3$ , which is in good agreement with the reduction peaks of CV curves, further demonstrating the typical electrochemical process of  $\alpha\text{-Fe}_2\text{O}_3$  [49,50]. The initial discharge/charge specific capacity of  $\alpha\text{-Fe}_2\text{O}_3@3\text{DrGO}$  reach up to  $1604.8$  and  $1020.7 \text{ mA h g}^{-1}$ , respectively, higher than the theoretical capacity ( $1007 \text{ mA h g}^{-1}$ ). The discharge/charge volumetric capacities of this  $\alpha\text{-Fe}_2\text{O}_3@3\text{DrGO}$  sample are calculated to be approximately  $481.4$  and  $306.2 \text{ mA h cm}^{-3}$ . However, the initial Coulombic efficiency is only  $63.6\%$  accompanied with a significant loss of irreversible capacity. Such a low Coulombic efficiency at first cycle may be attributed to that part of the iron oxide completes the reversible conversion reaction during the whole process. What's more, during the first discharge and charge process, partial electrolyte has been decomposed and the SEI film is formed at the solid-liquid interface between the electrode material and the electrolyte. Due to the partial consumption of the lithium ion in the electrolyte, this will inevitably lead to a lower Coulombic efficiency in the first cycle [39,47]. Nevertheless, the Coulombic efficiency of the 2nd cycle increases to  $93.5\%$  and remains above  $96.8\%$  in the following cycle. Even in the 60th cycle, the voltage windows of discharge/charge platforms almost keep the same, confirming the excellent reversibility of the electrochemical process of  $\alpha\text{-Fe}_2\text{O}_3@3\text{DrGO}$ . During the whole cycle process, the stable or increasing capacity indicates the effective

electron and ions transfer, or gradual activation in the  $\alpha\text{-Fe}_2\text{O}_3@3\text{DrGO}$  composite with the cycling [51].

Fig. 4b and c exhibit the different discharge/charge voltage profiles of  $\alpha\text{-Fe}_2\text{O}_3@3\text{DrGO}$  and  $\alpha\text{-Fe}_2\text{O}_3$  electrodes at various current density (from  $0.1 \text{ A g}^{-1}$  to  $5 \text{ A g}^{-1}$ ). Almost identical to Fig. 4a, a rapid drop ( $3\text{--}0.85 \text{ V}$ ), a plateau region ( $\sim 0.85 \text{ V}$ ) and one sloping region ( $0.75\text{--}0.01 \text{ V}$ ) appear in these curves, corresponding to different reaction process mentioned above. Meanwhile, we further analyze the capacity properties during the different reaction process by comparing these curves. In Fig. 4c, the significant attenuation phenomenon appears in both the plateau and sloping region with increasing the current density from  $0.1 \text{ A g}^{-1}$  to  $5 \text{ A g}^{-1}$ . This attenuation performance manifests that the bare  $\alpha\text{-Fe}_2\text{O}_3$  electrode cannot well maintain the conversion reaction and the surface interfacial reaction with rate increasing. When it refers to  $\alpha\text{-Fe}_2\text{O}_3@3\text{DrGO}$  electrode (Fig. 4b), the specific capacity maintains at a stable higher value than that of  $\alpha\text{-Fe}_2\text{O}_3$  electrode. Moreover, the platforms are almost similar to each other and the capacity corresponding to the sloping region are still higher than  $250 \text{ mA h g}^{-1}$  with weak decline, indicating the good surface interfacial lithium ion storage performance. Additionally, we also explore the gap of platform voltage between the conversion reaction process through the discharge/charge curves in Fig. S5. The polarization degree of electrode material can be recognized from the extent of change of this gap when it was tested at various current densities. It's clear

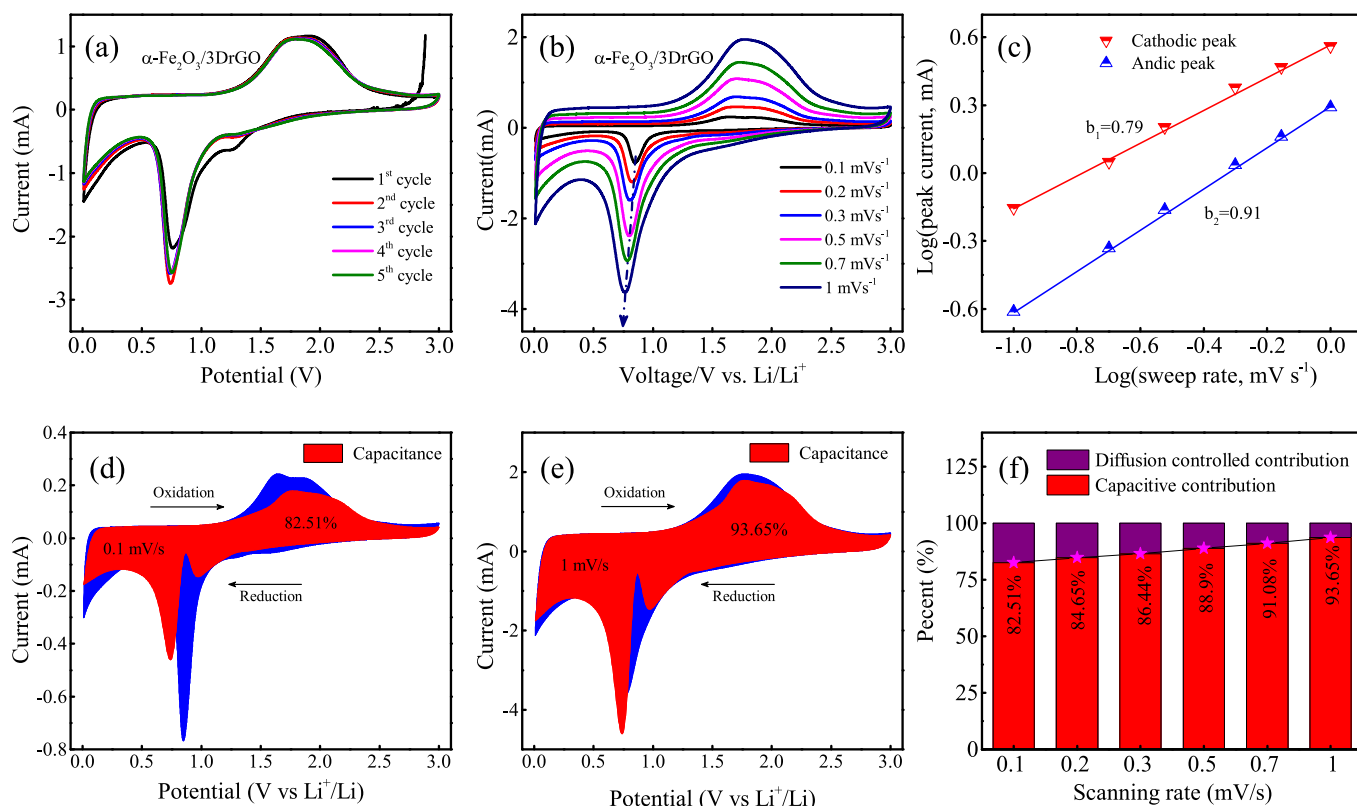


**Fig. 5.** CV characteristic and pseudocapacitance analysis for  $\alpha\text{-Fe}_2\text{O}_3@3\text{DrGO}$  electrode. (a) CV curves for initial 5 cycles at a scanning rate of  $0.5\text{ mV s}^{-1}$ ; (b) CV curves at various scanning rates between  $0.1$  and  $1\text{ mV s}^{-1}$ ; (c) Relationship between logarithm peak current and logarithm scanning rates; (d)–(e) the area that the pseudocapacitance take up in the total capacity at  $0.1$  and  $1\text{ mV s}^{-1}$ , respectively; (f) the contribution rate at various scanning rates ( $0.1\text{--}1\text{ mV s}^{-1}$ ) for the capacitive and diffusion controlled processes.

that the gaps of  $\alpha\text{-Fe}_2\text{O}_3$  electrode expand obviously, implying that the electrode takes place significant polarization with increasing the current density (varies from  $0.1\text{ A g}^{-1}$  to  $5\text{ A g}^{-1}$ ), especially under high current density. As for  $\alpha\text{-Fe}_2\text{O}_3@3\text{DrGO}$  electrode, there is almost bare change in the voltage gap against the change in current density, indicating a significantly strengthened electrochemical process without remarkable polarization in electrode material.

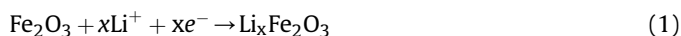
To better evaluate the electrochemical performance of  $\alpha\text{-Fe}_2\text{O}_3@3\text{DrGO}$ ,  $\alpha\text{-Fe}_2\text{O}_3$  and  $3\text{DrGO}$  electrodes, we further investigated their rate capability for 5 cycles at various current densities varying from  $0.1\text{ A g}^{-1}$  to  $5\text{ A g}^{-1}$ . As shown in Fig. 4d, the  $\alpha\text{-Fe}_2\text{O}_3@3\text{DrGO}$  electrode delivers the high and stable capacities at various current densities with only slightly dropping ( $1082.3$ ,  $1012.8$ ,  $966.4$ ,  $921.6$  and  $878.7\text{ mA h g}^{-1}$  at  $0.1$ ,  $0.2$ ,  $0.5$ ,  $1$  and  $2\text{ A g}^{-1}$ , respectively). It is noteworthy that this electrode still has a capacity of up to  $812.4\text{ mA h g}^{-1}$  at  $5\text{ A g}^{-1}$ , maintaining 75.1% of the initial reversible capacity at  $0.1\text{ A g}^{-1}$ . When the current density returns to  $0.1\text{ A g}^{-1}$ , the reversible capacity can be restored to  $942\text{ mA h g}^{-1}$  and it maintains and sustainably increases to  $1282.3\text{ mA h g}^{-1}$  after a short cycle of 30 laps, highlighting the outstanding lithium storage ability. In contrast, the bare  $\alpha\text{-Fe}_2\text{O}_3$  and  $3\text{DrGO}$  materials display dramatically decreased and lower capacity ( $129.5$  and  $154.3\text{ mA h g}^{-1}$  at  $0.5\text{ A g}^{-1}$ ,  $45.7$  and  $120.1\text{ mA h g}^{-1}$  at  $1\text{ A g}^{-1}$ ,  $3.3$  and  $77.8\text{ mA h g}^{-1}$  at  $5\text{ A g}^{-1}$ ) when the current rate was varied. It reveals that the  $\alpha\text{-Fe}_2\text{O}_3@3\text{DrGO}$  composite could not only maintain a stable electrochemical process, but also hold the ultra-fast charge transfer with abundant energy storage at varied current densities.

As we know, the cycle performance is also an important

criterion for their potential applications in the future LIBs field. The cycle performance of as-prepared electrodes and the coulombic efficiency of  $\alpha\text{-Fe}_2\text{O}_3@3\text{DrGO}$  nanocomposite were tested at a current density of  $1\text{ A g}^{-1}$  after activation for 5 cycles at  $0.1\text{ A g}^{-1}$  for a 200-cycle cycling, illustrated in Fig. 4e. Firstly, the  $\alpha\text{-Fe}_2\text{O}_3@3\text{DrGO}$  electrode delivers a higher specific capacity of  $914\text{ mA h g}^{-1}$  than that of  $\alpha\text{-Fe}_2\text{O}_3$  ( $285.9\text{ mA h g}^{-1}$ ) and  $3\text{DrGO}$  ( $143.7\text{ mA h g}^{-1}$ ) in the first cycle. Next, it goes through a slight fading down region, and the specific capacity gradually decreases to  $810.9\text{ mA h g}^{-1}$  after 38 cycles. However, in the range of 38–140 cycles, the capacity exhibits a steady rising state and stabilizes at  $1198.6\text{ mA h g}^{-1}$ . Finally, it keeps on this level up to 200 cycles. In Fig. S6, The discharge/charge voltage profiles for 140th, 160th, 180th and 200th cycle are almost identical to each other. What's more, the Coulomb efficiency maintains consistently at around 100% throughout the whole process. In contrast, the  $\alpha\text{-Fe}_2\text{O}_3$  and  $3\text{DrGO}$  electrode only shows the pretty low capacity of  $42.5$  and  $143\text{ mA h g}^{-1}$  after 200 cycles, far below the value of  $\alpha\text{-Fe}_2\text{O}_3@3\text{DrGO}$  composite. Notably, such a capacity fading-reativation phenomenon has been observed in our previous work [52–55] and it is common for metal oxide and carbon composite [56–59]. So far, there is no consistent conclusion to explain this phenomenon. This early capacity loss might be attributed to the partial decomposition of electrolyte and unstable SEI film. As the reaction proceeding, the electrolyte was evenly infiltrated and the so-called activation process could make the most use of electrode material. Then the electrode was gradually rearranged to provide more accessible active sites for lithiation reaction, developed more lithium ions transport channels, which brought about the increase of capacity in the consequent cycles [60].

Furthermore, on the electrode surface, the electrolyte degradation was kinetically activated and caused the reversible growth of the polymeric layer. This SEI film may provide additional lithium ion storage capacity. Meanwhile, the large specific surface area and porous 3D structure would significantly improve the so-called 'pseudocapacitance-type' lithium storage [61,62]. In addition, we also evaluated the long-term cycling stability at high current density ( $5 \text{ A g}^{-1}$ ) after 2000 cycles in Fig. 4g. As mentioned above, the partial decomposition of electrolyte and unstable SEI film resulted in the capacity decline in the initial stage. However, the  $\alpha\text{-Fe}_2\text{O}_3@3\text{DrGO}$  nanocomposite remained a stable reversible capacity of  $396.6 \text{ mA h g}^{-1}$  with nearly 100% Coulomb efficiency in the following cycling process, reflecting the fast and stable reversible reaction process for lithiation/delithiation process. Obviously, it is also superior to that of bare  $\alpha\text{-Fe}_2\text{O}_3$  or 3DrGO aerogel, implying that the synergetic effect between the 3D conductive graphene network with porosity and  $\alpha\text{-Fe}_2\text{O}_3$  nanoparticles can be responsible for the improved electrochemical performance in lithium storage. Meanwhile, we also conducted the cycle test on the  $\alpha\text{-Fe}_2\text{O}_3@3\text{DrGO}$  materials with different ratios of graphene and  $\alpha\text{-Fe}_2\text{O}_3$  and the results are shown in Fig. S7. Obviously, at the current density of  $1 \text{ A g}^{-1}$ , the cycle curves of the three electrodes with different composition ratios display the same tendency and exhibit excellent cycle performance. This further demonstrates that the three-dimensional porous aerogel prepared in this experiment are very beneficial for lithium storage. In particular, the products obtained by reacting 160 mg of graphene oxide with 3.2 mmol of ferric chloride possess the best electrochemical performance. Moreover, Fig. 4f and Table S1 show the comparisons of the rate and cyclic performance between  $\alpha\text{-Fe}_2\text{O}_3$  or 3DrGO composite and previously reported iron oxide based anode materials in the literature. Particularly, the  $\alpha\text{-Fe}_2\text{O}_3@3\text{DrGO}$  composite in this work exhibits high reversible capacity at different rates as well as a stable and long cycle life-span. All the above results well demonstrate that the  $\alpha\text{-Fe}_2\text{O}_3@3\text{DrGO}$  electrode can not only provide high interfacial Li-ion storage but also maintain an ultra-fast charge transfer rate to promote its performance at different current densities.

For a better investigation of the lithiation/delithiation behavior during the discharge/charge process, we conducted the cyclic voltammetry (CV) test of  $\alpha\text{-Fe}_2\text{O}_3@3\text{DrGO}$  and  $\alpha\text{-Fe}_2\text{O}_3$  in the voltage window of 0.01–3 V (vs.  $\text{Li}/\text{Li}^+$ ) at a scanning rate of  $0.5 \text{ mV s}^{-1}$  for 5 cycles. As shown in Fig. 5a and Fig. S8, the similar CV curves of these two electrodes reflect the similar electrochemical process. For the first cathodic scan (Fig. 5a), a strong reduction peak appears at the voltage of 0.75 V, corresponding to the reduction reaction of  $\text{Fe}^{3+}$  to  $\text{Fe}^0$ . And it is also accompanied by an irreversible reaction associated with the formation of a SEI film [63]. An additional minor peak observed at 1.28 V is ascribed to the Li insertion into the  $\alpha\text{-Fe}_2\text{O}_3$  nanocrystal.



For the first anodic scan, a clear broad peak consists of two extended peaks (1.75 and 1.96 V), which correspond to the oxidation of  $\text{Fe}^0$  to  $\text{Fe}^{2+}$  and further oxidation to  $\text{Fe}^{3+}$  [64]. After the first cycle, a slight offset happens to the cathodic peaks and the peak currents increase slightly, indicating the irreversible redox reaction in the initial lithiation/delithiation process accompanied by the light structural alteration with the minor polarization of electrode. It's noteworthy that the CV profiles are almost overlapped in the subsequent cycles, verifying the good electrochemical reversibility inducing to excellent cyclic performance. Meanwhile, we also measured the CV curves of  $\alpha\text{-Fe}_2\text{O}_3@3\text{DrGO}$  electrode at different scanning rate from 0.1 to  $1 \text{ mV s}^{-1}$  to explore the electrochemical kinetics and analyze the capacitive behavior in depth. As shown in

Fig. 5b, the peak voltage shifts toward the small voltage and the peak current increases with increasing the scanning rate, which means that the improved electrochemical kinetics in  $\alpha\text{-Fe}_2\text{O}_3@3\text{DrGO}$  electrode leads to high specific capacity. It's well known that the area enclosed by the CV curve represents the total lithium ion storage capacity. It consists of pseudocapacitance (derived from the charge-transfer process with surface or subsurface atoms), non-Faradaic contribution (induced by the double layer capacitive effect) and Faradaic contribution (derived from the  $\text{Li}^+$  diffusion controlled redox reaction process). The first two parts are collectively referred to the capacitive effect, which can be illuminated by the following equations [25,26].

$$i = a\nu^b \quad (2)$$

$$\log i = \log a + b \log \nu \quad (3)$$

where,  $i$  is the measured current and  $\nu$  represents the scanning rate. Adjustable parameter  $b$  can be determined from the slope of oblique line in  $\log(\nu)$ - $\log(i)$  plot. When  $b = 0.5$ ,  $i$  is proportional to the square root of the  $\nu$  and the charge transfer process is under the control of the diffusion-controlled process. When  $b = 1$ , the capacitive current occupies the primary contribution and the system is dominated by the capacitance process. Fig. 5c displays two oblique lines in the  $\log(V)$ - $\log(i)$  plot, corresponding to the oxidation and reduction processes of the CV curves, respectively. The values of  $b_1$  (oxidation process) and  $b_2$  (reduction process) are fitted to be  $\sim 0.79$  and  $0.91$  when the scanning rate varies from 0.1 to  $1.0 \text{ mV s}^{-1}$ . Obviously, both two  $b$  values are much closer to 1 instead of approaching to 0.5. Namely, the  $\alpha\text{-Fe}_2\text{O}_3@3\text{DrGO}$  electrode exhibits the surface-induced capacitive dominated mechanism. Therefore, the pseudocapacitance behavior must occupy a certain amount in the total lithium storage capacity. We can further quantitatively estimate the percentage of capacitive contribution according to the general relationship, [24].

$$i = k_1\nu + k_2\nu^{1/2} \quad (4)$$

where,  $k_1\nu$  represents the surface-induced capacitive effect part and  $k_2\nu^{1/2}$  reflects the diffusion-controlled redox reaction process, considering the current contribution. Therefore, as long as the values of the coefficients  $k_1$  and  $k_2$  are determined, we can quantify the current fractions corresponding to different mechanisms at every voltage. During the same electrochemical reaction, both  $k_1$  and  $k_2$  are fixed. Thus, we can get the value of  $k_1$  and  $k_2$  through the peak current under a same voltage to further obtain the different contribution rate in total lithium storage capacity for the surface-induced capacitive effect or diffusion-controlled process.

As presented in the red region of Fig. 5d and e, surface-induced capacitive contributions account for 82.51% and 93.65% at scanning rates of 0.1 and  $1 \text{ mV s}^{-1}$ , respectively, which derive from the surface of  $\alpha\text{-Fe}_2\text{O}_3@3\text{DrGO}$  electrode material. Moreover, the redox peaks are also clearly shown in these red regions, indicating that the surface-induced capacitive process is assigned to the pseudocapacitive behavior in this electrode. In Fig. 5f, more capacitive contribution occupy the dominated position with increasing the scanning rate. Due to the existence of numerous mesopores in this 3D porous architecture, only the capacitive process occurs on the surface of the electrode instead of the diffusion-controlled process, leading to boosted reaction kinetics and shortened ion transfer pathway. Hence, the excellent electrochemical characteristics at high current densities is dominated by a surface-induced pseudocapacitive effect in the  $\alpha\text{-Fe}_2\text{O}_3@3\text{DrGO}$  composite, guaranteeing both ultra-fast lithium ion and electron transfer and large power density in terms of lithium storage.

As we know, the EIS technology is also an effective method to explore the electrochemical kinetics of anode. We performed the EIS test in a frequency window from 100 KHz to 0.1 Hz, and the resulting Nyquist plots  $Z'$  vs.  $Z''$  of these as-prepared electrodes are compared in Fig. 6a. A typical impedance spectrum is generally composed of the intercept of the high frequency region, the suppressive semicircle of the high intermediate frequency region and the oblique portion of the low frequency region, which respectively correspond to the internal resistance ( $R_i$ ) (including resistance in electrolyte, contact resistance between particle with particle or between the electrode and the current collector, and diffusion resistance of the lithium ion passing through the SEI layer), the charge transfer resistance in interface between electrode and electrolyte ( $R_{ct}$ ), and the semi-infinite Warburg diffusion process of lithium ions in the electrode material ( $Z_w$ ). Obviously, the  $\alpha$ -Fe<sub>2</sub>O<sub>3</sub>@3DrGO electrode displays a more depressed semicircle and a more straight sloping line than the other two electrodes. It means a smaller  $R_{ct}$  and  $Z_w$ , which is ascribed to the superior morphology structure. The 3D interconnected porous GO network with extraordinary conductive properties serves as a conductive substrate, which are able to provide abundant highways for electron and lithium ion transfer. The  $\alpha$ -Fe<sub>2</sub>O<sub>3</sub> nanoparticles are homogeneously anchored on the inner and outer surfaces of the mesopores, realizing good contact between active materials with conductive carbon, strengthening the pseudocapacitive behavior. Ultimately, all these beneficial factors bring about the good electrochemical performance in LIBs consisting with above rate and cyclic performance. For a more intuitive understand of the diffusion of lithium ion inside the electrodes, the lithium ion diffusion coefficient ( $D_{Li}^+$ ) can be obtained by estimating the Warburg coefficient from the  $Z_{re}$  vs.  $\omega^{-1/2}$  plot in the low frequency region according to the following equations.

$$Z_{re} = R_{ct} + R_e + \sigma_w \omega^{-1/2} \quad (5)$$

$$D_{Li^+} = \frac{R^2 T^2}{2A^2 n^4 F^4 C^2 \sigma^2} \quad (6)$$

where,  $R_{ct}$ ,  $R_e$ ,  $\sigma_w$ ,  $\omega$ ,  $R$ ,  $T$ ,  $A$ ,  $n$ ,  $F$ ,  $C$  represent the electrode transfer

resistance, electrolyte resistance, the Warburg factor, frequency, gas constant, absolute temperature (in K), total surface area of electrode, the number of charge transfer, the Faraday constant and the concentration of lithium ions in electrode, respectively. Based on the above equations, as shown in Fig. 6b, the lithium ion diffusion coefficient of  $3.32 \times 10^{-12} \text{ cm}^2 \text{ s}^{-1}$  for  $\alpha$ -Fe<sub>2</sub>O<sub>3</sub>@3DrGO electrode is much higher than that for  $\alpha$ -Fe<sub>2</sub>O<sub>3</sub> electrode ( $9.96 \times 10^{-13} \text{ cm}^2 \text{ s}^{-1}$ ), suggesting that the anchor of  $\alpha$ -Fe<sub>2</sub>O<sub>3</sub> nanoparticles inside or outside of the porous structure cannot hinder the movement of lithium ions. In fact, the abundant mesopores in electrode could ensure sufficient space for lithium ion motion during the lithiation/delithiation process of Li<sup>+</sup> with Fe. The higher  $D_{Li}^+$  revealing the accelerated electron and ion transfer for  $\alpha$ -Fe<sub>2</sub>O<sub>3</sub>@3DrGO electrode through the tactfully construction of interconnected 3D porous architecture. To better understand the relationship among the electrochemical kinetics, micromorphology and cycle stability for  $\alpha$ -Fe<sub>2</sub>O<sub>3</sub>@3DrGO electrode after 200 cycles at 1 A g<sup>-1</sup>, the corresponding Nyquist, SEM, TEM figures are presented in Fig. 6c–f. As we can see, there is almost no change in the Nyquist plot before and after the cycling. The electrochemical kinetics are well maintained in the initial state. From the SEM and TEM images (Fig. 6d and e), the graphene oxide sheets are still clearly visible and they are connected to each other to form a three-dimensional framework with mesoporous. At the same time,  $\alpha$ -Fe<sub>2</sub>O<sub>3</sub> nanoparticles are still uniformly attached to the surface of the graphene oxide sheet, conducive to the pseudocapacitive storage. This indicates that after 200 cycles of cyclic testing, the 3D porous structure of the composite electrode undergoes partial structural rearrangement comparing to the cycling-test before, but the structure does not collapse, and it still keep the good structural integrity.

In the high-magnification TEM image (Fig. 6f), it could further confirm that the nanoparticles exhibit a dispersed state without agglomeration. We can clearly distinguish the interaction interface between graphene oxide sheets and iron oxide nanoparticles from the HRTEM image (Fig. 6g). Particularly, the interplanar spacing of 3.71 and 2.7 Å corresponds to the characteristic interlayer distance of (012) and (104) facets in  $\alpha$ -Fe<sub>2</sub>O<sub>3</sub> crystal. The TEM images analysis results imply that such porous graphene oxide network structure could provide a good stress relief and inhibit the agglomeration or pulverization during particle lithiation/

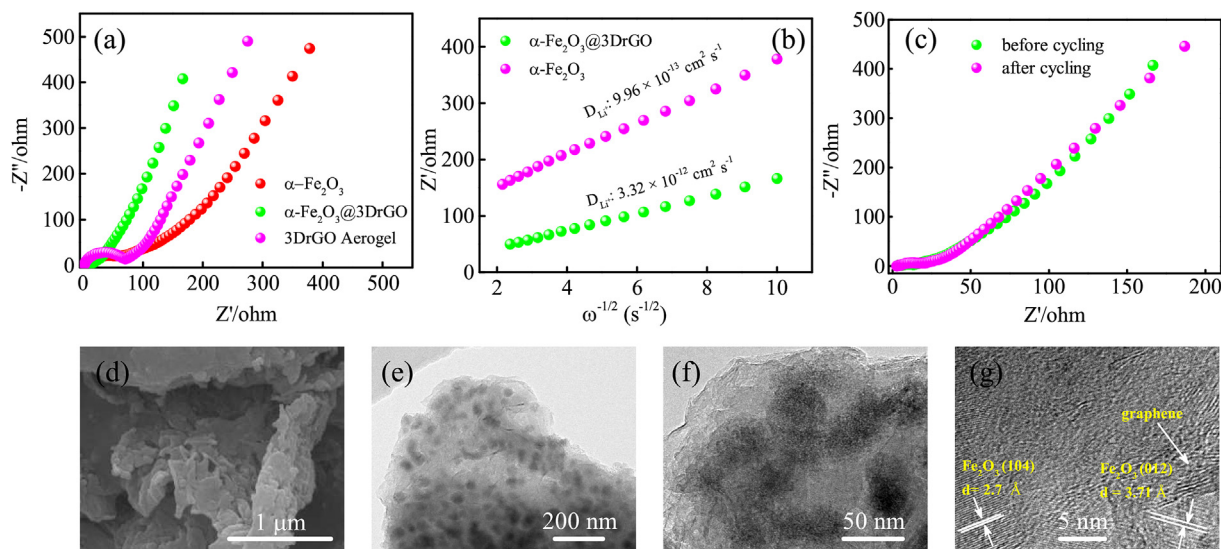


**Fig. 6.** (a) The Nyquist profiles of  $\alpha$ -Fe<sub>2</sub>O<sub>3</sub>@3DrGO,  $\alpha$ -Fe<sub>2</sub>O<sub>3</sub> and 3DrGO electrodes; (b) the  $Z_{re}$  vs.  $\omega^{-1/2}$  plot in the low frequency region for  $\alpha$ -Fe<sub>2</sub>O<sub>3</sub>@3DrGO and  $\alpha$ -Fe<sub>2</sub>O<sub>3</sub> electrodes; c The Nyquist profiles of  $\alpha$ -Fe<sub>2</sub>O<sub>3</sub>@3DrGO electrode before and after the 200th cycle at 1 A g<sup>-1</sup>; (d) SEM, TEM, high-magnification TEM, and HRTEM images for  $\alpha$ -Fe<sub>2</sub>O<sub>3</sub>@3DrGO electrode after the 200th cycle 1 A g<sup>-1</sup>.

delithiation process, further confirming the structural integrity. In a word, the desirable electrochemical performance of  $\alpha$ -Fe<sub>2</sub>O<sub>3</sub>@3DrGO composite could be attributed to the numerous merits of robust 3D interconnected porous framework. (i) The 3D interconnected reduced graphene oxide substrate with porosity is beneficial to electronic transfer due to itself outstanding conductive property. The robust mechanical flexibility can also effectively alleviate the volume expansion effect to ensure the structural stability. (ii) The numerous mesoporous with lager BET areas could promote the deeper penetration of the electrolyte, make the active material more fully contact with the electrolyte and provide multi-dimensional transmission pathways for electrons and lithium ions. (iii) The well-dispersed ultra-fine  $\alpha$ -Fe<sub>2</sub>O<sub>3</sub> particles and carbon framework are able to synergistically expand more accessible reaction sites, prevent the aggregation of  $\alpha$ -Fe<sub>2</sub>O<sub>3</sub>. Moreover, it exhibits the surface-induced capacitive dominated mechanism, which realizes the ultra-fast electrochemical reaction kinetics and guarantees excellent rate performance and long cycle lifespan.

#### 4. Conclusion

In summary, we have successfully synthesised a  $\alpha$ -Fe<sub>2</sub>O<sub>3</sub>@3DrGO aerogel with ultra-fine  $\alpha$ -Fe<sub>2</sub>O<sub>3</sub> nanocrystal well-anchored on inner and outside surface of 3D robust framework through a facial hydrothermal self-assembly process. It possesses multi-dimensional ultra-fast electron and lithium ion transport highways, abundant accessible reaction sites for lithiation/delithiation, and sufficient space to alleviate volume expansion. This composite exhibits an ultra-high initial specific capacity (1604.8 mA h g<sup>-1</sup>), excellent rate performance (921.6 mA h g<sup>-1</sup> at 1 A g<sup>-1</sup>, 812.4 mA h g<sup>-1</sup> at 5 A g<sup>-1</sup>) and steady rising cycle performance (1198.6 mA h g<sup>-1</sup> at 1 A g<sup>-1</sup> after 200 cycles) as well as remarkable cyclic lifetime (396.6 mA h g<sup>-1</sup> with nearly 100% Coulomb efficiency after 2000 cycles at 5 A g<sup>-1</sup>). All these excellent electrochemical performance could be contributed to the desirable 3D hierarchical porous structure, reduced polarization effect, fast rapid dynamic diffusion of lithium ions, and synergistic boosted ultra-fast pseudocapacitive kinetics. We believe that this study could provide one versatile method, which would bring the reference to the synthesis of other transition metal oxide-based composites with 3D porous structure for high power storage applications.

#### Acknowledgment

This work was financially supported by the National Natural Science Foundation of China (Grant Nos. 91833303, 61974043, and 61674057), the National Key R&D Program of China (Grant Nos. 2017YFA0303403 and 2018YFB0406500), the Projects of Science and Technology Commission of Shanghai Municipality (Grant Nos. 18JC1412400, 18YF1407200, and 18YF1407000), and the Program for Professor of Special Appointment (Eastern Scholar) at Shanghai Institutions of Higher Learning.

#### Appendix A. Supplementary data

Supplementary data to this article can be found online at <https://doi.org/10.1016/j.jallcom.2019.152627>.

#### References

- [1] L. Peng, Y. Zhu, D. Chen, R.S. Ruoff, G. Yu, Two-dimensional materials for beyond-lithium-ion batteries, *Adv. Energy Mater.* 6 (2016), 1600025.
- [2] C. Liu, F. Li, L.-P. Ma, H.-M. Cheng, Advanced materials for energy storage, *Adv. Mater.* 22 (2010) E28–E62.
- [3] J.B. Goodenough, *Electrochemical energy storage in a sustainable modern*

- society, *Energy Environ. Sci.* 7 (2014) 14–18.
- [4] X.X. Liu, D.L. Chao, D.P. Su, S.K. Liu, L. Chen, C.X. Chi, Y.Y. Lin, Z.X. Shen, J.P. Zhao, L.Q. Mai, Y. Lia, Graphene nanowires anchored to 3D graphene foam via self-assembly for high performance Li and Na ion storage, *Nano Energy* 37 (2017) 108–117.
- [5] X.X. Liu, Na. Li, C. Yang, Z. Liu, Y.Q. Feng, W.M. Dong, S.K. Liu, H. Liu, Y.L. Jia, J.P. Zhao, Y. Li, Sn accommodation in tunable-void and porous graphene bumper for high-performance Li- and Na-ion storage, *J. Alloy. Comp.* 790 (2019) 1043–1050.
- [6] Y. Cao, Y.X. Yang, Z.H. Ren, N. Jian, M.X. Gao, Y.J. Wu, M. Zhu, F. Pan, Y.F. Liu, H.G. Pan, A new strategy to effectively suppress the initial capacity fading of iron oxides by reacting with LiBH<sub>4</sub>, *Adv. Funct. Mater.* 27 (2017), 1700342.
- [7] N. Liu, Z. Lu, J. Zhao, M.T. McDowell, H.W. Lee, W. Zhao, Y. Cui, A pomegranate-inspired nanoscale design for large-volume-change lithium battery anodes, *Nat. Nanotechnol.* 9 (2014) 187–192.
- [8] Y.C. Dong, Z.Y. Zhang, Y. Xia, Y.-S. Chui, J.-M. Lee, J.A. Zapien, Green and facile synthesis of Fe<sub>3</sub>O<sub>4</sub> and graphene nanocomposites with enhanced rate capability and cycling stability for lithium ion batteries, *J. Mater. Chem. A* 3 (2015), 16206.
- [9] X.L. Zhang, X.X. Liu, C. Yang, N. Li, T.Y. Ji, K. Yan, B. Zhu, J.H. Yin, J.P. Zhao, Y. Li, A V<sub>2</sub>O<sub>5</sub>-nanosheets-coated hard carbon fiber fabric as high-performance anode for sodium ion battery, *Surf. Coat. Technol.* 358 (2019) 661–666.
- [10] O. Waser, M. Hess, A. Güntner, P. Novák, S.E. Pratsinis, Size controlled CuO nanoparticles for Li-ion batteries, *J. Power Sources* 241 (2013) 415.
- [11] Y.Z. Wu, P.N. Zhu, M.V. Reddy, B.V.R. Chowdari, S. Ramakrishna, Maghemite nanoparticles on electrospun CNFs template as prospective lithium-ion battery anode, *ACS Appl. Mater. Interfaces* 6 (2014) 1951–1958.
- [12] C. Xu, Y. Zeng, X. Rui, N. Xiao, J. Zhu, W. Zhang, J. Chen, W. Liu, H. Tan, H.H. Hng, Q. Yan, Controlled soft-template synthesis of ultrathin C@FeS nanosheets with high-Li-storage performance, *ACS Nano* 6 (2012) 4713–4721.
- [13] K.S. Lee, S.Y. Shin, T. Degen, W.Y. Lee, Y.S. Yoon, In situ analysis of SnO<sub>2</sub>/Fe<sub>2</sub>O<sub>3</sub>/RGO to unravel the structural collapse mechanism and enhanced electrical conductivity for lithium-ion batteries, *Nano Energy* 32 (2017) 397–407.
- [14] J.F. Zhang, L.J. Qi, X.S. Zhu, X.H. Yan, Y.F. Jia, L. Xu, D.M. Sun, Y.W. Tang, Proline-derived in situ synthesis of nitrogen-doped porous carbon nanosheets with encaged Fe<sub>2</sub>O<sub>3</sub>@Fe<sub>3</sub>C nanoparticles for lithium-ion battery anodes, *Nano Res.* 10 (2017) 3164–3177.
- [15] Y.J. Chen, X.H. Zhao, Y. Liu, A.A. Razzaq, A.K. Haridas, K.-K. Cho, Y. Peng, Z. Deng, J. Hyeon, Ahn,  $\gamma$ -Fe<sub>2</sub>O<sub>3</sub> nanoparticles aligned in porous carbon nanofibers towards long life-span lithium ion batteries, *Electrochim. Acta* 289 (2018) 264–271.
- [16] Y.J. Yoo, Y.J. Hong, Y.C. Kang, Rationally designed microspheres consisting of yolk-shell structured FeSe<sub>2</sub>-Fe<sub>2</sub>O<sub>3</sub> nanospheres covered with graphitic carbon for lithium-ion batteries, *J. Mater. Chem. A* 6 (2018), 15182.
- [17] M. Zhang, E.Z. Liu, T.T. Cao, H.Y. Wang, C.S. Shi, J.J. Li, C.N. He, F. He, L.Y. Ma, N.Q. Zhao, Sandwiched graphene inserted with graphene-encapsulated yolk-shell  $\gamma$ -Fe<sub>2</sub>O<sub>3</sub> nanoparticles for efficient lithium ion storage, *J. Mater. Chem. A* 5 (2017) 7035.
- [18] P. Santhoshkumar, K. Prasanna, Y.N. Jo, I.N. Sivagami, S.H. Kang, C.W. Lee, A facile and highly efficient short-time homogenization hydrothermal approach for the smart production of high-quality  $\alpha$ -Fe<sub>2</sub>O<sub>3</sub> for rechargeable lithium batteries, *J. Mater. Chem. A* 5 (2017), 16712.
- [19] P. Bhattacharya, M. Kota, D.H. Suh, K.C. Roh, H.S. Park, Biomimetic spider-web-like composites for enhanced rate capability and cycle life of lithium ion battery anodes, *Adv. Energy Mater.* (2017), 1700331.
- [20] J.S. Cho, Y.J. Hong, Y.C. Kang, Design and synthesis of bubble-nanorod-structured Fe<sub>2</sub>O<sub>3</sub>-carbon nanofibers as advanced anode material for Li-ion batteries, *ACS Nano* 4 (2015) 4026–4035.
- [21] X. Zhang, H.H. Liu, S. Petnikota, S. Ramakrishna, H.J. Fan, Electrospun Fe<sub>2</sub>O<sub>3</sub>-carbon composite nanofibers as durable anode materials for lithium ion batteries, *J. Mater. Chem. A* 2 (2014), 10835.
- [22] J. Jiang, Y. Li, J. Liu, X. Huang, C. Yuan, X.W. Lou, Recent advances in metal oxide-based electrode architecture design for electrochemical energy storage, *Adv. Mater.* 24 (2012) 5166–5180.
- [23] F. Feng, S. Zhao, R. Liu, Z. Yang, Q. Shen, NiO Flowerlike porous hollow nanostructures with an enhanced interfacial storage capability for battery-to-pseudocapacitor transition, *Electrochim. Acta* 222 (2016) 1160–1168.
- [24] D.L. Chao, C.R. Zhu, P.H. Yang, X.H. Xia, J.L. Liu, J. Wang, X.F. Fan, S.V. Saviolov, J.Y. Lin, H.J. Fan, Z.X. Shen, Array of nanosheets render ultrafast and high-capacity Na-ion storage by tunable pseudocapacitance, *Nat. Commun.* 7 (2016) 12122.
- [25] S. Li, J.X. Qiu, C. Lai, M. Ling, H.J. Zhao, S.Q. Zhang, Surface capacitive contributions: towards high rate anode materials for sodium ion batteries, *Nano Energy* 12 (2015) 224–230.
- [26] H.Y. Wang, H. Jiang, Y.J. Hua, P. Saha, Q.L. Cheng, C.Z. Li, Interface-engineered MoS<sub>2</sub>/C nanosheet heterostructure arrays for ultra-stable sodium-ion batteries, *Chem. Eng. Sci.* 174 (2017) 104–111.
- [27] D.L. Chao, P. Liang, Z. Chen, L.Y. Bai, H. Shen, X.X. Liu, X.H. Xia, Y.L. Zhao, S.V. Saviolov, J.Y. Lin, Z.X. Shen, Pseudocapacitive Na-ion storage boosts high rate and areal capacity of self-branched 2D layered metal chalcogenide nanoarrays, *ACS Nano* 10 (2016) 10211–10219.
- [28] V. Augustyn, J. Come, M.A. Lowe, J.W. Kim, P.L. Taberna, S.H. Tolbert, H.D. Abruna, P. Simon, B. Dunn, High-rate electrochemical energy storage through Li<sup>+</sup> intercalation pseudocapacitance, *Nat. Mater.* 12 (2013) 518–522.

- [29] C.J. Chen, Y.W. Wen, X.L. Hu, X.L. Ji, M.Y. Yan, L.Q. Mai, P. Hu, B. Shan, Y.H. Huang, Na<sup>+</sup> intercalation pseudocapacitance in graphene-coupled titanium oxide enabling ultra-fast sodium storage and long-term cycling, *Nat. Commun.* 6 (2015) 6929.
- [30] X.H. Xia, D.L. Chao, Y.Q. Zhang, J.Y. Zhan, Y. Zhong, X.L. Wang, Y.D. Wang, Z.X. Shen, J.P. Tu, H.J. Fan, Generic synthesis of carbon nanotube branches on metal oxide arrays exhibiting stable high-rate and long-cycle sodium-ion storage, *Small* 12 (2016) 3048–3058.
- [31] H. Qi, L.Y. Cao, J.Y. Li, J.F. Huang, Z.W. Xu, Y.Y. Cheng, X.G. Kong, K. Yanagisawa, High pseudocapacitance in FeOOH/rGO composites with superior performance for high rate anode in Li-ion battery, *ACS Appl. Mater. Interfaces* 8 (2016) 35253–35263.
- [32] Y. Xiang, Z.G. Yang, S.P. Wang, Md. Shahriar A. Hossain, J.X. Yu, N.A. Kumar, Y. Yamauchi, Pseudocapacitive behavior of the Fe<sub>2</sub>O<sub>3</sub> anode and its contribution to high reversible capacity in lithium ion batteries, *Nanoscale* 10 (2018), 18010.
- [33] W.S. Hummers, R.E. Offeman, Preparation of graphitic oxide, *J. Am. Chem. Soc.* 80 (1958), 1339–1339.
- [34] Y. Wang, X.M. Guo, Z.K. Wang, M.F. Lv, B. Wu, Y. Wang, C. Yan, A.H. Yuan, H.X. Yang, Controlled pyrolysis of MIL-88A to Fe<sub>2</sub>O<sub>3</sub>@C nanocomposites with varied morphologies and phases for advanced lithium storage, *J. Mater. Chem. A* 5 (2017), 25562.
- [35] L. Liu, X.F. Yang, C.X. Lv, A.M. Zhu, X.Y. Zhu, S.J. Guo, C.M. Chen, D.J. Yang, Seaweed-derived route to Fe<sub>2</sub>O<sub>3</sub> hollow nanoparticles/N-doped graphene aerogels with high lithium ion storage performance, *ACS Appl. Mater. Interfaces* 8 (2016) 7047–7053.
- [36] Y.L. Ding, C. Wu, P. Kopold, P.A. van Aken, J. Maier, Y. Yu, Graphene-protected 3D Sb-based anodes fabricated via electrostatic assembly and confinement replacement for enhanced lithium and sodium storage, *Small* 11 (2015) 6026–6035.
- [37] F.Y. Jin, Y. Wang, Topotactical conversion of carbon coated Fe-based electrodes on graphene aerogels for lithium ion storage, *J. Mater. Chem. A* 3 (2015) 14741–14749.
- [38] P. Li, Y. Ding, A. Wang, L. Zhou, S. Wei, Y. Zhou, Y. Tang, Y. Chen, C. Cai, T. Lu, Self-assembly of tetrakis (3-trifluoromethylphenoxy) phthalocyaninato cobalt(II) on multiwalled carbon nanotubes and their amperometric sensing application for nitrite, *ACS Appl. Mater. Interfaces* 5 (2013) 2255–2260.
- [39] T.C. Jiang, F.X. Bu, X.X. Feng, I. Shakir, G.L. Hao, Y.X. Xu, Porous Fe<sub>2</sub>O<sub>3</sub> nano-frameworks encapsulated within three-dimensional graphene as high-performance flexible anode for lithium-ion battery, *ACS Nano* 11 (2017) 5140–5147.
- [40] D.H. Liu, H.Y. Lu, X.L. Wu, B.H. Hou, F. Wan, S.D. Bao, Q.Y. Yan, H.M. Xie, R.S. Wang, Constructing the optimal conductive network in MnO-based nanohybrids as high-rate and long-life anode materials for lithium-ion batteries, *J. Mater. Chem. A* 3 (2015) 19738–19746.
- [41] X. Wang, X. Cao, L. Bourgeois, H. Guan, S. Chen, Y. Zhong, D.M. Tang, H. Li, T. Zhai, L. Li, N-doped graphene-SnO<sub>2</sub> sandwich paper for high-performance lithium-ion batteries, *Adv. Funct. Mater.* 22 (2012) 2682–2690.
- [42] W.Y. Yuan, J. Yuan, J.L. Xie, C.M. Li, Polymer-mediated self-assembly of TiO<sub>2</sub>@Cu<sub>2</sub>O core-shell nanowire array for highly efficient photoelectrochemical water oxidation, *ACS Appl. Mater. Interfaces* 8 (2016) 6082–6092.
- [43] S.Y. Li, Y.Y. Liu, P.S. Guo, C.X. Wang, Self-climbed amorphous carbon nanotubes filled with transition metal oxide nanoparticles for large rate and long lifespan anode materials in lithium ion batteries, *ACS Appl. Mater. Interfaces* 9 (2017) 26818–26825.
- [44] B.H. Xu, X.G. Guan, L.Y. Zhang, X.W. Liu, Z.B. Jiao, X.H. Liu, X.Q. Hu, X.S. Zhao, A simple route to preparing γ-Fe<sub>2</sub>O<sub>3</sub>/RGO composite electrode materials for lithium ion batteries, *J. Mater. Chem. A* 6 (2018) 4048.
- [45] L. Qu, Y. Liu, J.B. Baek, L. Dai, Nitrogen-Doped graphene as efficient metal-free electrocatalyst for oxygen reduction in fuel cells, *ACS Nano* 4 (2010) 1321–1326.
- [46] R. Lv, T. Cui, M.S. Jun, Q. Zhang, A. Cao, D.S. Su, Z. Zhang, S.H. Yoon, J. Miyawaki, I. Mochida, Open-ended N-doped carbon nanotube-graphene hybrid nanostructures as high-performance catalyst support, *Adv. Funct. Mater.* 21 (2011) 999–1006.
- [47] Y. Jin, L. Dang, H. Zhang, C. Song, Q. Lu, F. Gao, Synthesis of unit-cell-thick α-Fe<sub>2</sub>O<sub>3</sub> nanosheets and their transformation to γ-Fe<sub>2</sub>O<sub>3</sub> nanosheets with enhanced LIB performances, *Chem. Eng. J.* 326 (2017) 292–297.
- [48] H. Xia, D.D. Zhu, Y.S. Fu, X. Wang, CoFe<sub>2</sub>O<sub>4</sub>-graphene nanocomposite as a high-capacity anode material for lithium-ion batteries, *Electrochim. Acta* 83 (2012) 166–174.
- [49] L.S. Xiao, M. Schroeder, S. Kluge, A. Balducci, U. Hagemann, C. Schulz, H. Wiggers, Direct self-assembly of Fe<sub>2</sub>O<sub>3</sub>/reduced graphene oxide nanocomposite for high-performance lithium-ion batteries, *J. Mater. Chem. A* 3 (2015), 11566.
- [50] Y.Z. Wang, J.S. Han, X.X. Gu, S. Dimitrijević, Y.L. Hou, S.Q. Zhang, Ultrathin Fe<sub>2</sub>O<sub>3</sub> nanoflakes using smart chemical stripping for high performance lithium storage, *J. Mater. Chem. A* 5 (2017), 18737.
- [51] Y.J. Zhao, X.M. Zhai, D. Yan, C.H. Ding, N. Wu, D.Z. Su, Y.Z. Zhao, H.P. Zhou, X.C. Zhao, J.B. Li, H.B. Jin, Rational construction the composite of graphene and hierarchical structure assembled by Fe<sub>2</sub>O<sub>3</sub> nanosheets for lithium storage, *Electrochim. Acta* 243 (2017) 18–25.
- [52] M.J. Li, Q.L. Deng, J.Y. Wang, K. Jiang, L.Y. Shang, Z.G. Hu, J.H. Chu, In-situ gas reduction in reversible SnS-SnO<sub>2</sub>@N-doped graphene anodes for high-rate and lasting lithium storage, *J. Alloy. Comp.* 769 (2018) 1007–1018.
- [53] C. Wu, J.Y. Wang, Q.L. Deng, M.J. Li, K. Jiang, L.Y. Shang, Z.G. Hu, J.H. Chu, Pseudocapacitive Li-ion storage boosts high-capacity and long-life performance in multi-layer CoFe<sub>2</sub>O<sub>4</sub>/rGO/C composite, *Nanotechnology* 30 (2019), 045401.
- [54] J.Y. Wang, Q.L. Deng, M.J. Li, C. Wu, K. Jiang, Z.G. Hu, J.H. Chu, Facile fabrication of 3D porous MnO@GS/CNT architecture as advanced anode materials for high-performance lithium-ion battery, *Nanotechnology* 29 (2018), 31540.
- [55] J.Y. Wang, Q.L. Deng, M.J. Li, K. Jiang, Z.G. Hu, J.H. Chu, High-capacity and long-life lithium storage boosted by pseudocapacitance in three-dimensional MnO-Cu-CNT/graphene anodes, *Nanoscale* 10 (2018) 2944.
- [56] Y.Z. Jiang, D. Zhang, Y. Li, T.Z. Yuan, N. Bahlawane, C. Liang, W.P. Sun, Y.H. Lu, M. Yan, Amorphous Fe<sub>2</sub>O<sub>3</sub> as a high-capacity, high-rate and long-life anode material for lithium ion batteries, *Nano Energy* 4 (2014) 23–30.
- [57] S. Zhu, J.J. Li, X.Y. Deng, C.N. He, E.Z. Liu, F. He, C.S. Shi, N.Q. Zhao, Ultrathin-Nanosheet-induced synthesis of 3D transition metal oxides networks for lithium ion battery anodes, *Adv. Funct. Mater.* 27 (2017), 1605017.
- [58] J.E. Lee, S.-H. Yu, D.J. Lee, D.-C. Lee, S.I. Han, Y.-E. Sung, T. Hyeon, Facile and economical synthesis of hierarchical carbon-coated magnetite nanocomposite particles and their applications in lithium ion battery anodes, *Energy Environ. Sci.* 5 (2012) 9528.
- [59] W. Wei, S.B. Yang, H.X. Zhou, I. Lieberwirth, X.L. Feng, K. Müllen, 3D graphene foams cross-linked with pre-encapsulated Fe<sub>3</sub>O<sub>4</sub> nanospheres for enhanced lithium storage, *Adv. Mater.* 25 (2013) 2909.
- [60] J.L. Cheng, B. Wang, C.-M. Park, Y.P. Wu, H. Huang, F.D. Nie, CNT@Fe<sub>3</sub>O<sub>4</sub>@C coaxial nanocables: one-pot, additive-free synthesis and remarkable lithium storage behavior, *Chem. Eur. J.* 19 (2013) 9866.
- [61] S. Grugeon, S. Laruelle, L. Dupont, J.M. Tarascon, An update on the reactivity of nanoparticles Co-based compounds towards Li, *Solid State Sci.* 5 (2003) 895.
- [62] J.S. Do, C.H. Weng, Preparation and characterization of CoO used as anodic material of lithium battery, *J. Power Sources* 146 (2005) 482.
- [63] D. Larcher, D. Bonnin, R. Cortes, I. Rivals, L. Personnaz, J.-M. Tarascon, Studies of the reduction by lithium of α-Fe<sub>2</sub>O<sub>3</sub> with various particle sizes, *J. Electrochem. Soc.* 150 (2003) A1643–A1650.
- [64] K. Cao, L. Jiao, H. Liu, Y. Liu, Y. Wang, Z. Guo, H. Yuan, 3D hierarchical porous α-Fe<sub>2</sub>O<sub>3</sub> nanosheets for high-performance lithium-ion batteries, *Adv. Energy Mater.* 5 (2015), 1401421.